Soft Matter

Diffusion, Density, and Defects on Spheres

SCHOLARONE™
Manuscripts

Diffusion, Density, and Defects on Spheres

John E. Bond,* Alex J. Yeh,* John R. Edison, Michael A. Bevan†
Chemical & Biomolecular Engr., Johns Hopkins Univ., Baltimore, MD 21218 USA

Abstract

We simulate and model diffusion of spherical colloids of radius, *a*, on spherical surfaces of radius, *R*, as a function of relative size and surface concentration. Using Brownian Dynamics simulations, we quantify diffusion and microstructure at different concentrations ranging from single particles to dense crystalline states. Self-diffusion and structural metrics (pair distribution, local density, and topological charge) are indistinguishable between spheres and planes for all concentrations up to dense liquid states. For concentrations approaching and greater than the freezing transition, smaller spheres with higher curvature show increased diffusivities and nonuniform density/topological defect distributions, which differ qualitatively from planar surfaces. The total topological charge varies quadratically with sphere radius for dense liquid states and linearly with sphere radius for dense crystals with icosahedrally organized grain scars. Between the dense liquid and dense crystal states on spherical surfaces is a regime of fluctuating and interacting defect clusters. We show local density governs self-diffusion in dense liquids on flat and spherical surfaces via the pair distribution. In contrast, dynamic topological defects couple to finite diffusivities through freezing and in low density crystal states on spherical surfaces, where neither exist on flat surfaces.

keywords: self-diffusion | colloids | Brownian Dynamics | curvature | topological defects

Introduction

Finding colloidal particles far from any surface is exceedingly rare, and the vast majority of these surfaces are not flat. In analogy to atoms forming nano- tube and closed ball morphologies,[1] or adsorbing to complex pore surfaces,[2] colloidal species can adsorb and assemble onto curved surfaces in diverse materials and applications. Assembling nano- and micro- scale components into or onto spherical surfaces include viral capsids,[3] vesicles,[4] cell membranes,[5] Pickering emulsion drops,[6] colloidosomes,[7] pollens,[8] insect eyes,[9] liquid marbles,[10] multicellular organisms,[11] blastula, organoids,[12] etc. Examples of other common material applications and environments with curved surfaces involving adsorbed/assembled colloidal species include particles in porous media (soil, oil reservoirs, tumor vasculature), tissue surfaces, and bacterial colonies. In each of these applications, the behaviors and properties of colloidal ensembles depend on their interactions, dynamics, and structures as they are confined to fixed or often flexible substrate surfaces with underlying curvature.

While the behavior and properties of spherical colloidal particles on flat surfaces are generally well understood, many aspects of spherical particles on curved surfaces have yet to be reported. For example, colloids with short-range repulsion on planar surfaces have quasi-2D phase behavior well approximated by predictions for 2D hard disks.[13-16] They exhibit uniform liquid states below a melting concentration and hexagonal crystals above a freezing concentration. However, simply trying to wrap a 2D crystal around a sphere is not possible without introducing defects,[8] which is a basic example of geometric frustration.[17] According to the Euler-Poincarè

---

† To whom correspondence should be addressed. email: mabevan@jhu.edu
* These authors contributed equally to this work.

theorem, any hexagonal lattice on a sphere must contain at least twelve 5-coordinated particles within the otherwise 6-coordinated crystal, however finding specific solutions for equilibrium particle configurations must involve minimizing the free energy with respect to particle interactions (*e.g.* the Thomson and Tammes problems).[8] The role of curvature in governing geometrically frustrated equilibrium structures leads naturally towards more general open problems involving phase behavior, diffusive dynamics, non-equilibrium behavior, and ultimately emergent properties (*e.g.*, mechanical, electrical, optical, etc.) in curved colloidal systems.

Phase behavior and defect types for spherical colloidal particles on spherical surfaces is unknown for arbitrary temperatures, interactions, concentrations, and relative dimensions, but specific problems have been addressed in models and experiments. For a 2D elastic solid at zero temperature, defects are predicted to organize as twelve grain scars (instead of flat 2D grain boundaries) distributed with icosahedral symmetry on sphere surfaces (*e.g.*, like soccer balls). Each of the twelve grain scars consists of chains of connected 5- and 7- coordinated particles with one excess 5- coordinated particle, which satisfies the Euler-Poincarè theorem. These chains' length depends linearly on the ratio of lattice spacing ($2a$) to sphere size (R).[18] This prediction has been validated for colloidal particles adsorbed at spherical drop oil-water interfaces with repulsive dipolar potentials. Such systems visibly forms grains scars whose length depends linearly on relative dimensions ($R/2a$)[19] and whose positions exhibit icosahedral symmetry.[20] In contrast, experiments on colloids with short-range attractive interactions adsorbed to spherical drop interior surfaces produce dendritic crystals due to elastic instabilities.[21] Other simulation studies have revealed additional defect motifs for particles on spherical surfaces vs. particle number.[22] Beyond the static organization of near-equilibrium low energy crystal state defects, numerous open questions remain about equilibrium and non-equilibrium structures, defects, and dynamics.

Colloidal diffusion on spherical surfaces has received little attention, whether it be within equilibrium states or as part of non-equilibrium dynamics. In contrast, 2D diffusion on flat surfaces is relatively well understood. For example, concentration dependent diffusion in flat colloidal monolayers[23] agrees with established self-diffusion models.[24] In brief, diffusion approaches the 2D Stokes-Einstein value at infinite dilution, decreases monotonically with increasing liquid concentration,[25] and decreases more significantly upon crystallization before vanishing with further densification.[26] On flat surfaces, self-diffusion in liquids is coupled to 2D static structural features.[27] Whereas in crystal states, dislocations can enable finite diffusivities.[28] The expectation is that that structural features like curvature mediated defects may impact diffusion on spheres. For particles on spheres, even single particle diffusion requires a different model to capture 3D localization,[29-31] which must be carefully considered before addressing packing effects and defects. Studies of concentrated particle dynamics on spheres include dislocation dynamics within grain scars,[32] curvature-dependent spatially heterogeneous glassy relaxation,[33] and melting dynamics unaffected by grain scars.[34] While these latter studies probe how grain scars mediate some dynamics within crystal states, they do not provide comprehensive characterization of particle diffusion.

In this work, we measure self-diffusion in Brownian Dynamics (BD) simulations of spherical colloids on spherical surfaces as a function of relative size and surface concentration (**Fig. 1**). We consider short-range screened electrostatic repulsive potentials so that particles behave as effective 2D hard spheres or hard disks. We compare concentration dependent self-diffusion on spherical and planar surfaces from infinite dilution through freezing up to dense crystal states. We then compare measured diffusivities to structural metrics related to density and
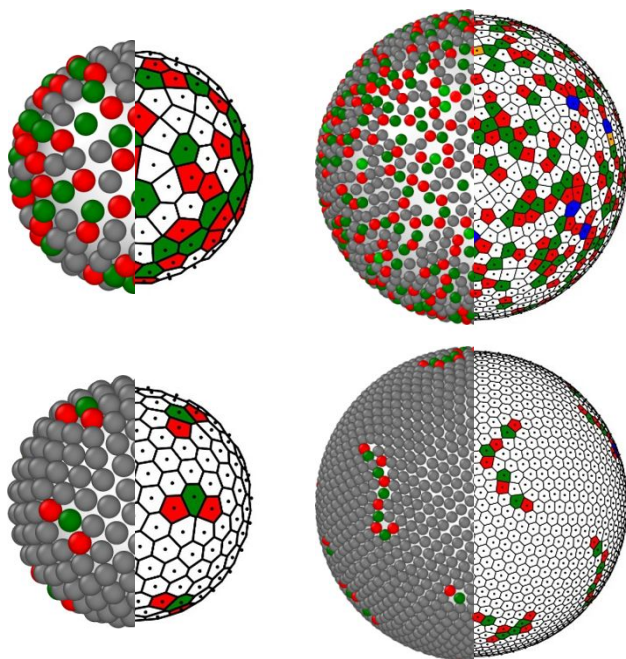
Fig 1. Effective hard spheres on different sized spheres. (**top**) At low area fractions, there are no obvious ordered microstructures in liquid states based on tessellations and coloring particles by their coordination number (see Fig.6C legend for color scheme). (**bottom**) At high area fractions, hexagonal crystalline states are obtained with icosahedrally organized grain scars each with one excess 5-coordinated particle. Note grain scar length is ~3 particles for small sphere and ~10 particles for larger sphere.

topological defects to gain insights into mechanisms controlling particle diffusion in liquid and crystal states on both spherical and planar surfaces. While findings from these results are intended to describe colloidal diffusion on spherical surfaces relevant in numerous applications, they are also generalizable to molecular systems.

Results & Discussion

Self-Diffusion on Planes & Spheres

We use Brownian Dynamics to simulate spherical particles of radius a on both planar surfaces and spherical surfaces of varying radii, R, and varying surface concentrations (**Fig. 2**). We investigate a screened electrostatic repulsive potential, $U(r)=A\exp(-\kappa r)$, that is very short-ranged compared to particle dimensions ($\kappa a >> 1$). This short-range potential is realistic for typical aqueous charged colloids, is easily compatible with BD simulations, and allows us to capture 2D phase behavior with a by hard disk model using a perturbation theory.[35] Practically, we can treat particles with core radii, a, as having an effective radius, a_{eff}, and effective area fraction based on the 2D particle number density, $\eta=\rho\pi a_{\text{eff}}^2$. Because system size, area fraction, and spherical substrate radius are coupled, in the following we choose a range of $R/2a$ values and particle area fractions of interest, which determine system sizes that we also use as benchmark cases for flat BD simulations at the same conditions.

We first illustrate how to measure the self-diffusivity, D, from BD trajectories using the mean squared displacement, $\langle r^2 \rangle$, vs. time, t on a single spherical surface radius and on a flat surface with the same particle number (**Fig. 2**). For all planar and spherical surface concentrations, as $t \rightarrow 0$, measured data are well captured by,
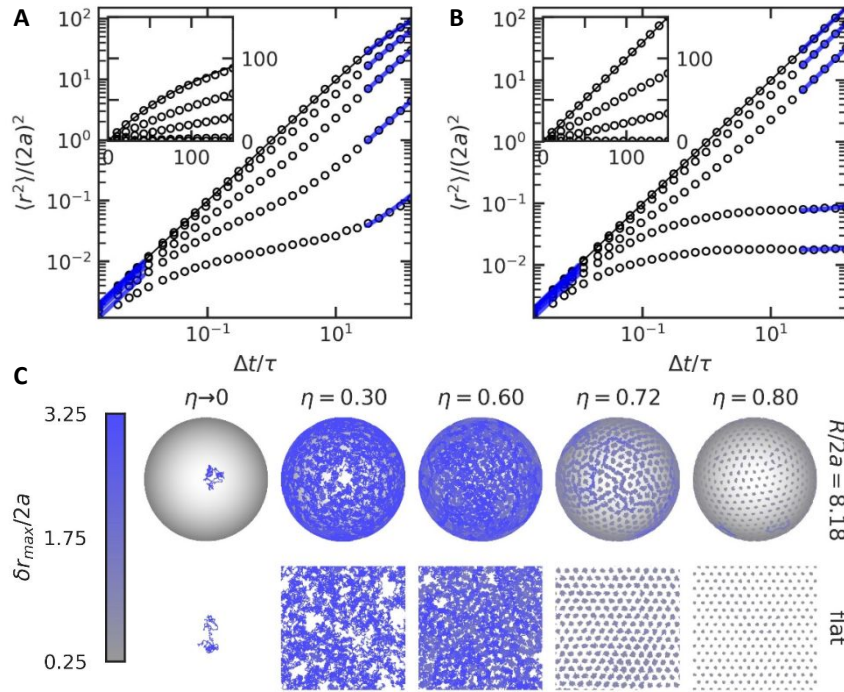
Fig 2. Measuring diffusion from simulated trajectories on spherical and planar surfaces. For particles on a (**A**) flat surface with periodic boundary conditions, and (**B**) a spherical surface with $R/2a$=8.18, Euclidean mean squared displacements are shown for area fractions of (top-to-bottom) η = 0, 0.3, 0.6, 0.72, 0.8. Insets show the same data on linear scales. D_0 is obtained in all cases by fitting Eq. (1) to simulated data as $t \rightarrow 0$. D_L is obtained for flat surfaces by fitting Eq. (1) to simulated data for $t>10\tau$. D_L is obtained for spherical surfaces by fitting Eq. (2) to simulated data for $t>10\tau$. (**C**) Rendered trajectories over 14τ are colored by each particle's maximum displacement to contrast (blue) mobile particles and (gray) localized particles.

$$\left\langle r^2 \right\rangle = 4D\Delta t \tag{1}$$

where D in this limit is the Stokes-Einstein diffusivity, $D_0=kT/6\pi\mu a$, where kT is the product of Boltzmann's constant and absolute temperature and the medium has viscosity μ. In the BD equation of motion we specify that the diffusivity be D_0, and so we expect Eq. (1) to recover the input diffusivity at very short-times. Indeed, we see that D_0 is the short-time self-diffusivity in all cases. If we had chosen to include hydrodynamic interactions, the short-time self-diffusivity would instead be the trace of the multi-body diffusion tensor;[24] which manifests as a concentration-dependent scalar that does not influence diffusion at longer times.

In contrast to the short-time self-diffusion behavior observed on both spherical and planar surfaces (**Fig. 2**), at longer times the diffusivity approaches different, concentration-dependent, values. On the planar surface, the $\langle r^2 \rangle$ vs. t data exhibit a well-defined long-time linear region fit by Eq. (1), where D now refers to the concentration dependent long-time self-diffusivity, D_L. On the spherical surface, 3D confinement yields long-time $\langle r^2 \rangle$ vs. t data captured by a different functional form,[29-31]

$$\left\langle r^2 \right\rangle = 2R^2 \left[1 - \exp\left(2D\Delta t / R^2 \right) \right] \tag{2}$$

where $\langle r^2 \rangle$ is calculated using Euclidean displacements. Observe that Eq. (2) approaches Eq (1) as $t \rightarrow 0$, as expected. While $D=D_0$ accurately captures single particle diffusion ($\eta \rightarrow 0$) on spheres (**Fig. 2B**), we must fit Eq. (2) to long-time data to obtain D_L as a function of concentration. The results for both planar and spherical substrates show D_L decreases as η increases. However, the long-time $\langle r^2 \rangle$ vs. t data plateaus for $\eta > 0.7$ on planar surfaces but not on spherical surfaces. The plateau indicates D_L vanishes with freezing on planar surfaces, just as expected,[26] but remains nonzero on spherical surfaces at the same area fraction and particle number.

Rendered particle trajectories (**Fig. 2C**) appear indistinguishable for liquid states ($\eta < 0.7$) on both spherical and planar surfaces. However, the crystal states ($\eta > 0.7$) on the spherical substrate retain significant diffusion over length scales greater than the particle and lattice dimension. This contrasts heavily with flat systems at the same area fraction which only exhibit localized lattice motion and no significant diffusion. These observations from the rendered trajectories confirm the long-time diffusion apparent in the $\langle r^2 \rangle$ vs. t data in the spherical vs. planar substrate results for crystal states ($\eta > 0.7$). The presence of diffusing particles at crystalline area fractions suggests that surface curvature enables dynamic processes not possible on flat surfaces at otherwise identical conditions. However, these high-η dynamics are spatially heterogeneous, and as such are not strictly long-time *self*-diffusion as it is defined. Therefore, the spatially averaged long-time diffusivity, D_L, measures both the self-diffusive process when $\eta<0.7$ and spatially heterogeneous diffusion when $\eta>0.7$. To clarify terminology, we will refer to D_L as the *apparent* diffusivity when it reflects high-η, spatially heterogeneous diffusion.

Analysis of Measured Self-Diffusivities

To investigate how curvature influences colloidal diffusivities, we perform additional BD simulations and diffusion measurements similar to the results reported in **Fig. 2** on a range of differently sized spherical surfaces and concentrations, as well as on planar surfaces with the same concentrations and particle numbers. **Fig. 3** summarizes measured D_L values normalized by the short-time diffusivities (*i.e.*, D_0) as D_L/D_0 in plots over the full η range, which a focus on the vicinity where D_L vanishes. For reference, we include vertical lines for hard disk melting and freezing (from very large system size simulations[16]) and a horizontal line based on a 2D dynamic freezing criterion.[26] Our data approach the intersection of the vertical freezing/melting lines and the horizontal dynamic freezing criterion line, although we cannot expect to exactly match the vertical lines since these are for essentially infinite system sizes. Correspondence of our results with these independent estimates/constraints indicates consistency with established hard disk phase behavior and freezing dynamics.

Additionally, our results correspond with a previously verified microstructural description of long-time self-diffusion in concentrated 2D colloidal liquid states with attractive and repulsive interaction potentials[24] (originally developed for concentrated 3D colloidal dispersions[25]). This additional theoretical line in **Fig. 3** is given as,

$$D_L/D_0 = \left[1 + 2\eta g(2a)\right]^{-1} \tag{3}$$

where $g(2a)$ is the height of the first peak of the pair distribution function (where $g(r)=\rho(r)/\langle\rho\rangle$). According to Eq. (3) the ratio of the long-time and short-time diffusivities depends on the product of the average concentration η and $g(2a)$, which is practically the average first-coordination shell density. Eq. (3) captures the data well for $\eta < 0.5$, above which additional terms are needed for more concentrated liquids.[36] For $\eta < 0.65$, the measured diffusivities are the same across five
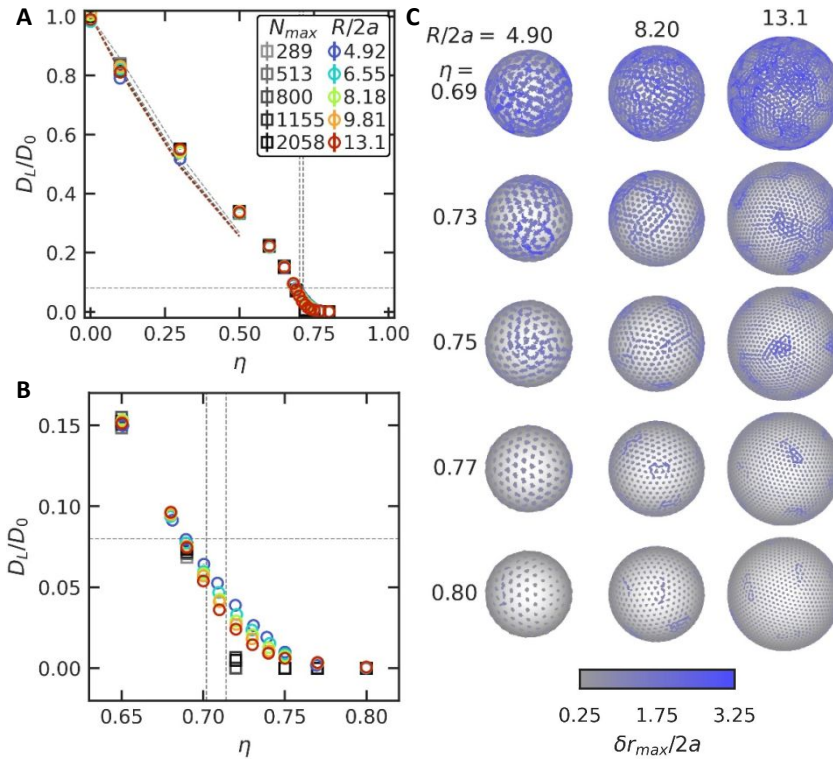
Fig 3. Summary of self-diffusion vs. concentration and curvature. (**A**) Concentration dependent long-time diffusivity, D_L, normalized by short-time value, D_0. Dashed lines indicate Eq. (3), (horizontal) dynamic freezing criterion,[26] and (vertical) infinite system size hard-disc freezing/melting transitions.[16] (**B**) High-density data zoom view of data in panel A. (**C**) Rendered trajectories colored by maximum Euclidean displacement over fixed time (gray-blue scale) for different $R/2a$ and η.

different flat-case system sizes and five different spherical surface sizes. For $\eta > 0.65$, the flat surface diffusivities vanish as η approaches the freezing transition, but all spherical surface apparent diffusivities remain nonzero, and the spectrum color scale indicates higher apparent diffusivities for spherical surfaces with smaller radii and higher curvatures

With the summary of results in **Fig. 3**, along with guidance from theoretical expectations, several key trends emerge. The trend in D_L/D_0 from infinite dilution up to high density liquid states is independent of substrate curvature and agrees with established models for 2D self-diffusion. However, as the system approaches freezing from the dense liquids, the trend in D_L/D_0 begins to depend on substrate curvature and persists for spherical surfaces up to very high area fractions ($\eta \sim 0.8$). Rendered trajectories (**Fig. 3C**) show only a subset of particles diffusing past their neighbors and through their first coordination shell. Furthermore, the spatial organization of particles with higher diffusivities increasingly takes on the icosahedral symmetry reminiscent of the grain scar ground state in elastic solids on spherical surfaces. Interestingly, symmetry begins to emerge at much lower concentrations than we expect to form well-defined grain scars. In the following sections we focus on understanding the origin of the combined curvature and concentration dependent diffusion observed in **Fig. 3**.

Spatial Density Variations

  Given the success of local density for explaining D_L/D_0 in homogeneous dense liquid states on both flat and curved surfaces (*e.g.* Eq. (3)), we next examine more closely density variations as a mechanism for explaining the curvature dependent D_L/D_0 in **Fig. 3**. The ensemble average pair distribution function for each curved and flat system (**Fig. 4A**) shows all cases collapse to indistinguishable curves for $\eta < 0.71$, but for higher concentrations there is a curvature-dependence that is most pronounced in the height of the first peak, $g(2a)$. However, plotting the right-hand side of Eq. (3) with the measured $g(2a)$ (**Fig. 5A**) yields a trend where higher curvatures systematically indicate lower diffusivities, which is opposite to the measured trend (**Fig. 3**). No simple extension of Eq. (3) to higher concentrations can resolve this incorrect curvature dependence, which indicates that ensemble average microstructure, despite having a curvature dependence, does not relate to diffusivity in the same manner as for concentrated liquid states. Given that particles on spherical surfaces split into mobile and immobile populations (**Fig. 3C**), it is perhaps unsurprising that ensemble averaging does not capture the apparent diffusivity dominated by a small sub-population.

  To consider how local density influences diffusivities of sub-populations, we use tessellation to define the area fraction for each particle, $\eta_i = \pi a^2/A_i$, where A_i is the area of its Voronoi polygon. Tessellations on spheres and planes show polygons colored by local area fraction, η_i (**Fig. 4C**). Time-averaged histograms, $p(\eta_i)$ are, again, curvature independent for liquid states but show noticeable curvature-dependent distributions for crystal states (**Fig. 4B**). For crystal states on spherical surfaces, the distributions are skewed towards higher values, indicating
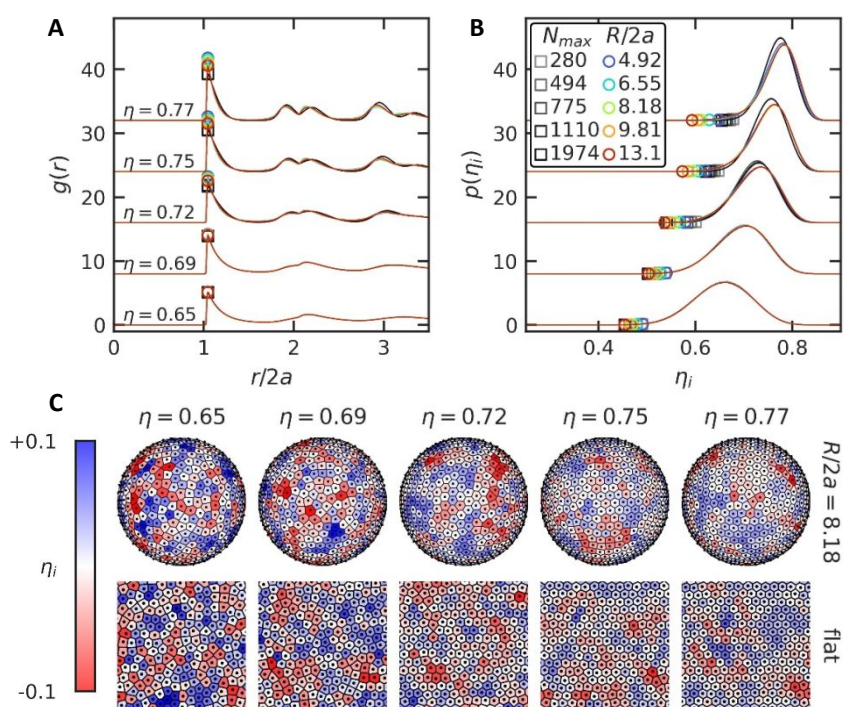

Fig 4. Measures of local particle density on flat and spherical surfaces. (**A**) Pair distribution functions collapse for all liquid states but show curvature-dependent first peak for crystal states. (**B**) Local density histograms for same average concentrations as in panel A collapse for liquid states but have skew towards higher local densities in crystal states. Points indicate η_{min} defined as time-average of lowest local η_i in every configuration. (**C**) Visualization of local concentration, η_i, for use in panel B using Voronoi tessellation.

more particles have higher local η_i. These same distributions also have a longer low-η tail on spherical surfaces compared to flat surfaces. These curvature-dependent low-η tails are the best-case scenario for local density as a descriptor of the curvature-dependent diffusivities. We define the time-average minimum area fraction, η_{min}, to characterize this tail. Because D_L is expected to vanish at a critical concentration as $\sim(1-\eta/\eta_C)$,[25] we plot $(1-\eta_{min}/0.907)$ vs. η for all flat and spherical surface cases (**Fig. 5B**) to see if this has a similar scaling to the D_L/D_0 vs. η trends in **Fig. 3**. There is a weak system-size dependence in η_{min} for the gray-scale planar data, however, crystal states on spherical surfaces do not collapse to their flat-case counterparts, and in fact have a larger spread compared to flat-case data. The larger, less curved spheres have a lower η_{min} that would appear to suggest higher D_L, but this is again opposite to the trend in **Fig. 3B**, showing local low-density fluctuations do not capture the curvature dependent D_L data.

By locally averaging the density per particle, η_i, in a particle-sized area around each point on the sphere and over a short time window (**Fig. 5C**), spatial variations are captured that are not obvious from statistical data alone (**Fig. 4**). As the ensemble average η increases, the local η spatial variations transition from relatively small and random to icosahedrally distributed, persistent, low-density regions. The low-η regions necessitate that other regions have higher local η. These high-η regions are consistent with the skew towards high densities in the curvature-dependent crystal state $g(2a)$ (**Fig. 4A**) and density histograms (**Fig. 4B**). The magnitude and organization of the red low-η regions provides a visual cue for η_{min} being relatively lower in more crystalline states with
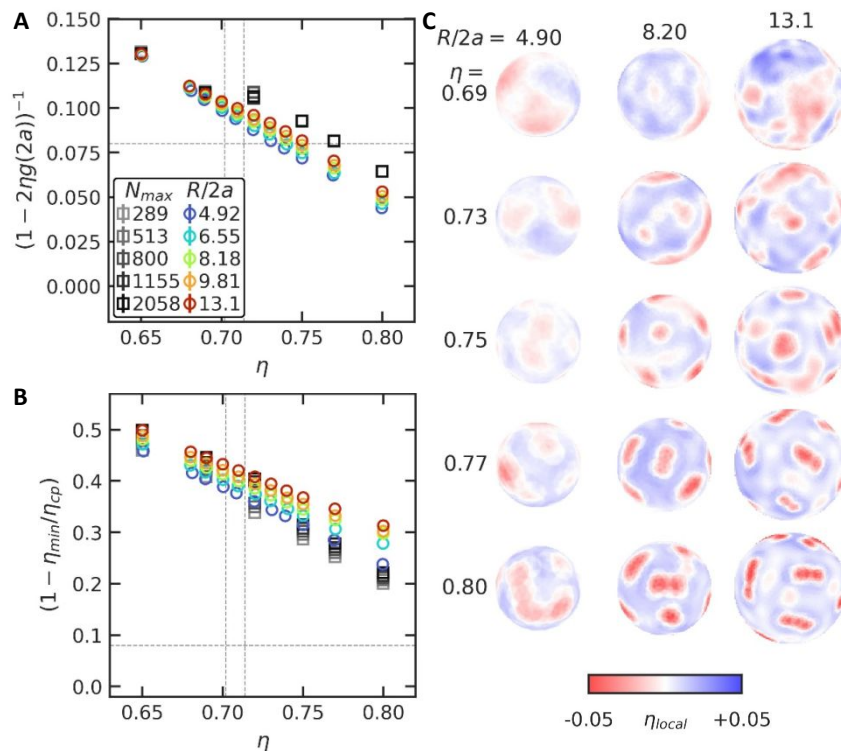

Fig 5. Scaling curvature and concentration dependent density metrics. (**A**) Plotting the right hand side of Eq. (3) based on measured curvature and concentration dependent pair distribution functions. (**B**) Plotting alternate scaling quantity for possible vanishing behavior of D_L (see text) based on measured time-average minimum local area fraction. (**C**) Local η_i time-averaged (14τ) and space-averaged ($2.5\pi[2a]^2$) to visualize spatial density variations vs. curvature and concentration

higher $R/2a$. Since the most skewed part of the local density distribution (η_{min}) has the wrong curvature dependence, other properties of the local density distributions like their variance and skewness logically follow. These collective observations show density variations are insufficient to explain the curvature-dependent D_L/D_0, particularly because curvature dependent density trends are opposite to what is needed to account for the curvature-dependent diffusivity trends. However, the low-density regions appear to emerge with the icosahedral symmetry expected for crystal state grain scars (at least for the higher $R/2a$ cases at the highest densities), which suggests we look more carefully into connections between topological defect metrics and curvature-dependent D_L/D_0.

Curvature & Concentration Dependent Topological Charge

We next quantify topological defects for all cases on flat and spherical surfaces as a function of concentration. For 2D hexagonal crystals, a topologically defective particle is any particle whose coordination number is not six. Following convention,[8] we define each particle's topological charge, q_i, and an ensemble total charge, Q, as,

$$q_i = 6 - c_i, \quad Q = \Sigma |q_i| \tag{4}$$

where c_i, is each particle's coordination number as determined from a Voronoi tessellation (**Fig. 6C**). From definitions in Eq. (4), the η-dependence of the total charge is shown for both flat (**Fig. 6A**) and spherical surfaces (**Fig. 6B**). Results show an expected system size dependence, where more particles yield more defects. For all cases, at low concentrations ($\eta \lesssim 0.5$), there are few
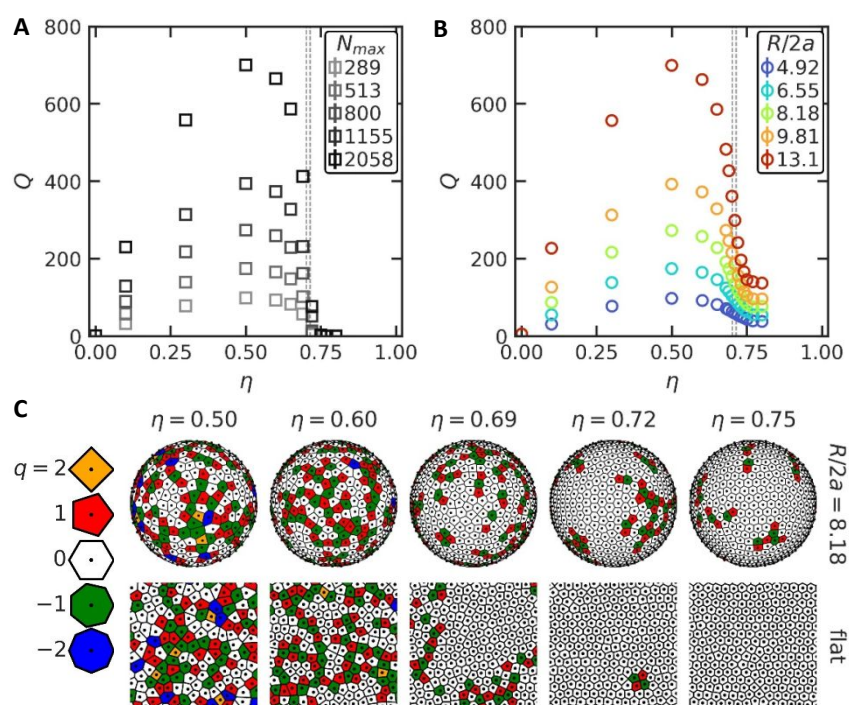

Fig 6. Coordination number and topological charge vs. concentration and curvature. The total topological charge, given by Eq. (4) applied to Voronoi tessellations of the (**A**) plane and (**B**) sphere, shows characteristic system-size dependence. (**C**) Example renderings showing coordination number and topological charge of each particle for flat and curved systems, in support of visualizing the high-density trends in panels A and B.

particles and little order, so coordination number and topological charge are random and Q increases with increasing concentration. Further increasing concentration ($\eta \gtrsim 0.5$) causes particles to more closely pack, which causes Q to decrease with increasing positional order as the system approaches freezing. At the usual freezing condition, Q vanishes for all flat cases but remains nonzero with a curvature dependence for spherical surfaces.

To support these observations, high-η renderings (**Fig. 6C**) reveal that spherical crystals retain clusters of topological charges to capture how Q approaches a nonzero value for those cases. Furthermore, the spectral spread (**Fig. 6B**) shows a clear systematic curvature dependence for Q in the high-η limit. Taken together, these observations are reminiscent of the trends in the apparent long-time diffusive behavior in **Fig. 2**. Below the freezing transition the spherical and planar cases behave similarly. Approaching and beyond the freezing transition on the sphere, both Q and D_L retain a qualitatively different, nonzero, curvature-dependence in contrast to flat systems.

Normalizing the total charge, Q, (**Fig. 6**) by the particle number, N, accounts for the aforementioned system size dependence and highlights the similarity between the trends in defect population and diffusivity (**Fig. 7**). Plotting Q/N collapses all flat and spherical surface cases for the same area fractions that had identical self-diffusivities (**Fig. 7A**). While all flat cases collapse through freezing, spherical cases exhibit curvature-dependence around freezing (**Fig. 7B**). Time- and space- averaged renderings of the local charge density, Q/N, (**Fig. 7C**) show low-η cases have isotropic defect densities, whereas the onset of crystalline order breaks the spherical rotational
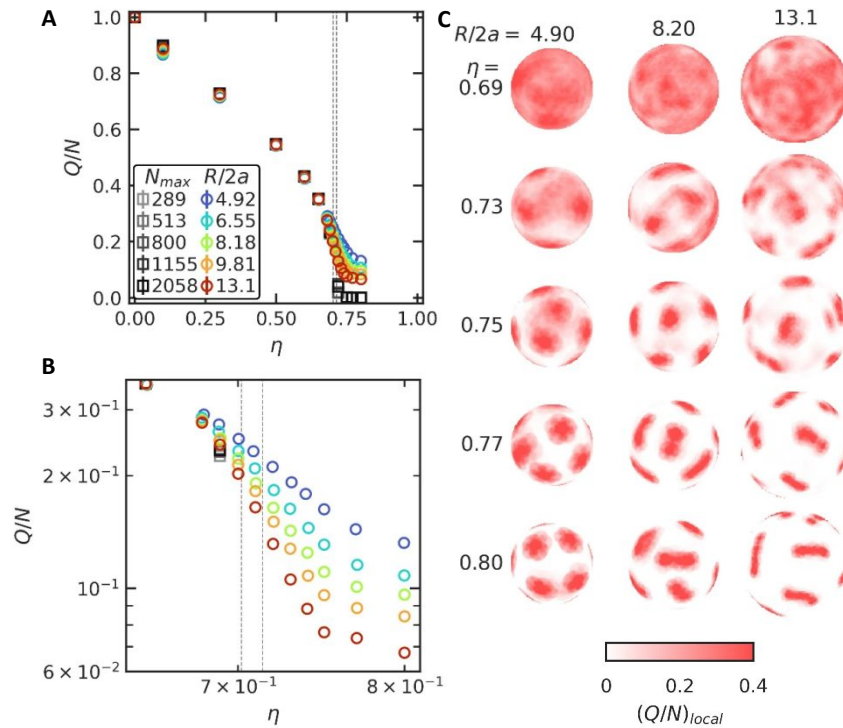

Fig 7. Summary of ensemble average total topological charge vs. concentration and curvature. (A) Normalizing total charge (Eq. (4)), Q, by ensemble size, N, collapses for dense liquids to near freezing conditions (vertical lines). **(B)** Near and beyond freezing, the flat case charge density vanishes, but the sphere-case is nonzero and curvature dependent. **(C)** Renderings of time-averaged (14τ) and space-averaged ($2.5\pi[2a]^2$) local charge density, show charge density is constant and isotropic in liquid states. Icosahedral symmetry emerges through freezing, before culminating in linearly oriented grain scars.[18]

symmetry so that high charge density regions localize with icosahedral symmetry. The inherent defect symmetry causes the inhomogeneous η profile (**Fig. 5C**) where 5- and 7- coordinated particles necessarily pack less efficiently than 6- coordinated particles, thus producing lower local η. The curvature dependent Q/N (**Fig. 7A**) has the same trend as the curvature dependent D_L/D_0 (**Fig. 3A**) at all η, including independence for liquid states and higher values for smaller $R/2a$. This contrasts with the opposite curvature dependence of local density metrics (**Figs. 5A,B**) compared to D_L/D_0, and suggests that the distribution of topological defects is important for understanding diffusion in crystal states and near freezing conditions.

Correlating Diffusivity & Defects

Focusing on high-η states on spheres, particles with the highest diffusivities (**Fig. 3**) appear to have the same curvature dependence and spatial organization as particles with the highest charge density (**Fig. 7**). These observations, and guidance from results in prior studies,[28, 32] lead to the expectation that particles with the highest diffusivities are associated with topological defects. Consider how curvature dependent D_L/D_0 scales with the fraction of defective particles. In the limit that only frequently defective particles have nonzero diffusivity and predominantly crystalline particles have vanishing diffusivity, the ensemble average apparent diffusivity becomes the fraction of defective particles times their diffusivity. Then, since the average defect fraction and degree is simply Q/N, the observed D_L/D_0 should scale with Q/N. Plotting (D_L/D_0) from **Fig. 3** divided by (Q/N) from **Fig. 7** collapses all data onto a curvature independent trend that smoothly
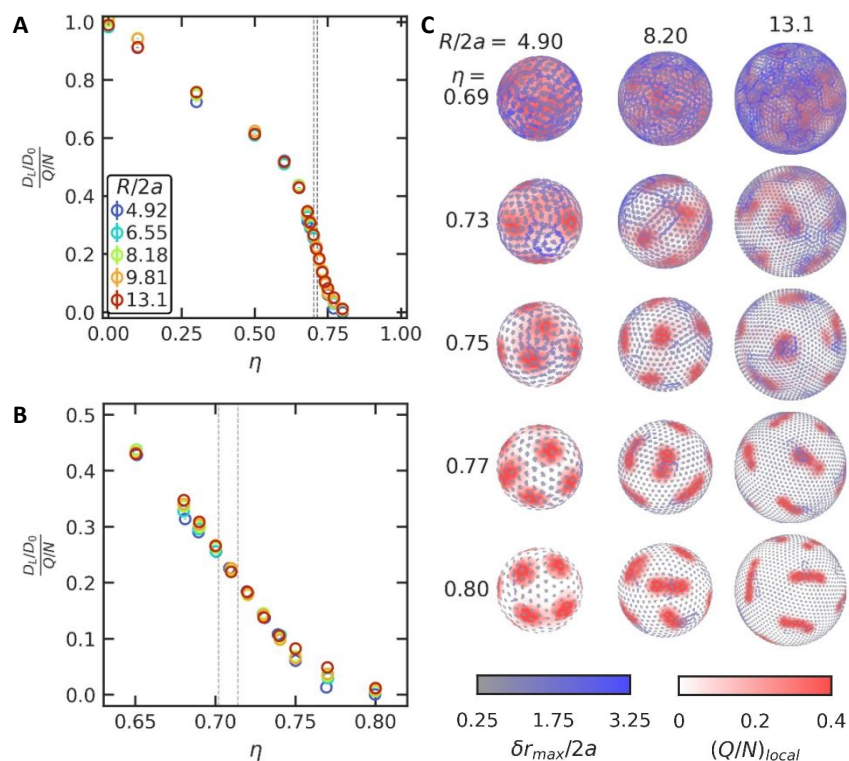

Fig 8. Correlating curvature and concentration dependent diffusivity and defects. (**A**) Dividing the normalized long-time diffusivity, D_L/D_0, by charge density, Q/N, removes curvature dependence, including (**B**) zoom view of freezing region, where all other quantities in **Figs. 3-7** display curvature dependence. (**C**) Overlaying time averaged maximum Euclidean displacements and local charge density for the same time window reveals the mobile particles generally colocalize with defective crystal regions with exceptions.

transitions from unity at infinite dilution through freezing and vanishes at high densities (**Fig. 8**). The scaling in **Fig. 8** is particularly successful at accounting for all curvature dependence in the freezing region and beyond.

In addition to connecting the common scaling of D_L/D_0 and Q/N (**Figs. 8A, B**), we also visually assess the spatial correlations in the two quantities by overlaying (**Fig. 8C**) for the same time window the max displacement data (**Fig. 3C**) and local charge density data (**Fig. 7C**). At densities just below freezing (for flat, infinite systems; η=0.69), blue trajectories show that particles can isotropically escape local nearest-neighbor cages, and these trajectories lay on a relatively isotropic background charge density. At densities well beyond freezing (η=0.8), the majority of particles are localized on lattice positions, and the small proportion of particles that display the largest displacements occur in the high charge density regions. Between these limiting cases, the longest bluest trajectories consistently lie on top or near the red high charge density regions (*e.g.*, $R/2a$=13.1, η=0.75 is especially clear) and localized gray trajectories lie in the white low charge density regions of perfect crystal. Interestingly, a number of cases show less co-localization of large diffusive displacements and high charge density, and in some even less frequent observations capture highly mobile particles between defect-rich regions (*e.g.*, $R/2a$=8.2, η=0.73). These observations show that longer-time collective diffusive motion enabled by defect regions does not imply exact correspondence between the most diffusive and most defective particles. However, the clear collapse of the data in **Figs. 8A,B** that captures all curvature dependent trends indicates a clear mechanistic coupling between the most diffusive and most defective particles.

Curvature & Concentration Dependent Defects

We explore the curvature dependence of defective particles in different states to better understand curvature dependent apparent diffusivity via their coupling in **Fig. 8**. Curvature-dependent defect populations fall between the limits of isotropic liquid states at low η and dense crystals with grain scars at high η (**Fig. 7**). In liquid states, curvature-independent charge density arises because the defect population is isotropic, such that total charge, Q, is proportional to particle number and thus sphere surface area. Using the fact that liquid state charge densities are identical for flat and sphere surfaces (**Fig. 7**), the curvature dependent total charge for liquid states on the spheres, $Q_{S,\mathrm{liq}}$, is given as,

$$
\begin{aligned}
(Q/N)_{S,liq} &= (Q/N)_{F,liq} = \alpha(\eta) \\
Q_{S,liq} &= \alpha(\eta) N_{S,liq} = \alpha(\eta)(\eta/\pi a^2)(4\pi R^2) = \alpha(\eta)16\eta(R/2a)^2
\end{aligned}
\tag{5}
$$

which has no adjustable parameters, given we can measure the concentration dependent liquid charge density on flat surfaces, $\alpha(\eta)=(Q/N)_{F,\mathrm{liq}}$ (**Fig. 7A**). Eq. (5) accurately captures simulated curvature-dependent total charge for liquid states on different sized spheres (**Fig. 9A**).

In high-η crystal states, twelve linearly oriented and icosahedrally organized grain scars arise from balancing curvature-induced lattice deformation against the cost of defect formation. Each grain scar has a 'length' determined by the number of extra 5-7 dislocations attached to each of the twelve 5-fold disclinations.[18] The length in number of dislocations per disclination, n_D, is related to the total charge due to scars, $Q_{S,\mathrm{scar}}$, and the non-dimensional sphere-particle radii, $R/2a$, by (solving for n_D or $Q_{S,\mathrm{scar}}$),

$$n_D \equiv (1/2)\left[\left(Q_{S,scar}/12\right)-1\right] = 0.41\left(R-R_C\right)/2a$$

$$Q_{S,scar} = 24\left(n_D+1/2\right) = 24\left[0.41\left(R-R_C\right)/2a+1/2\right]$$

(6)

where R_C, is a critical radius dependent on the crystal elastic constants. Eq. (6) captures the linear scaling of Q vs. $R/2a$ at $\eta=0.8$ (**Fig. 9B**). While Eq. (6) is only strictly valid at zero temperature, additional defects 'proliferate' at finite temperature,[8, 18] which manifests as a slightly greater slope
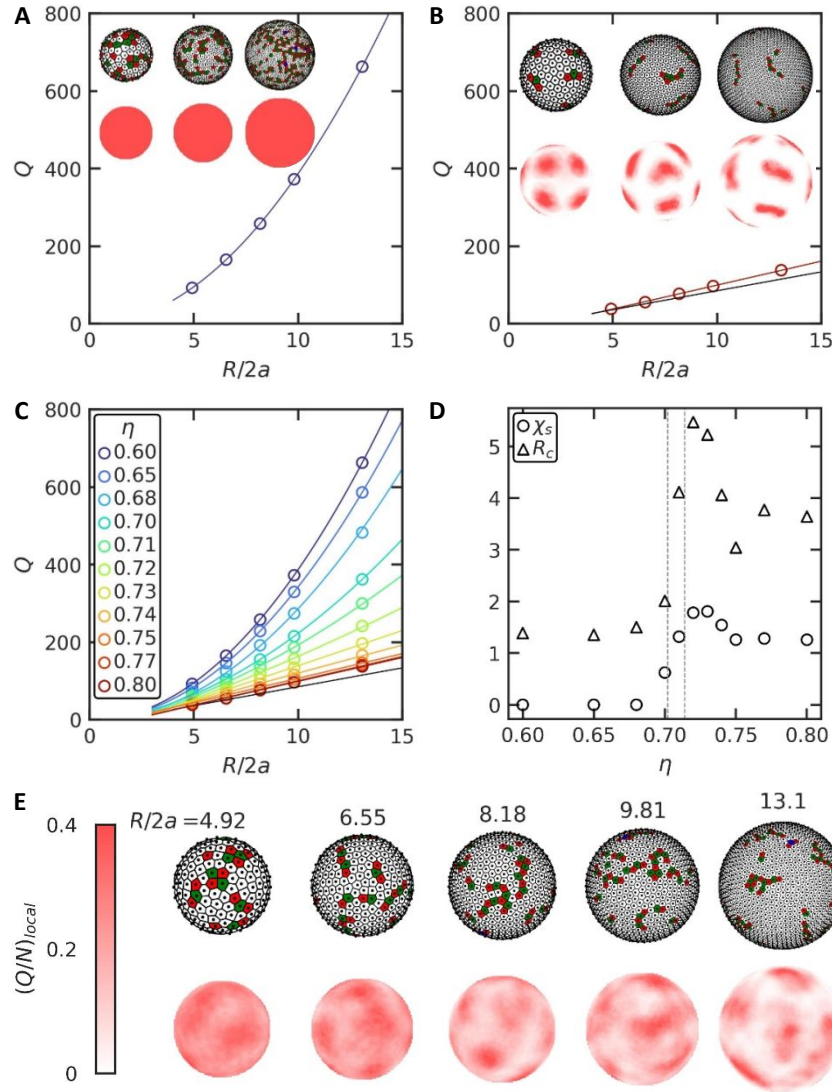

Fig 9. Quantification of curvature & concentration dependent defects. Total charge, Q, (Eq. (4)) vs. $R/2a$ from BD simulations for (**A**) liquid state area fraction of η = 0.6 and model line from Eq. (5), (**B**) crystal state area fraction of η = 0.8 and model line from Eq. (6), and (**C**) all concentrations between η = 0.6-0.8 with model line from Eq. (7) with two adjustable parameters, plotted in (**D**) showing transition from χ=0 for liquids to χ=1 for static grain scars, critical radius, R_C, values required for χ>0. In addition to inset renderings in panels A and B show representative tessellations and time averaged local charge density, the same rendering types are shown in (**E**) for η=0.73 to visualize twelve interacting disclination centers, which corresponds to non-monotonic peak values of χ, R_C, in panel D.

in **Fig. 9B**, as previously reported.[33] Inset renderings in **Fig. 9B** show anisotropic local charge density and tessellations, which capture the increasing length of grain scars via additional dislocations as the sphere radius increases. The time-averaged anisotropic morphology of high-charge-density regions shows the relatively static localization of grain scars. In this regime, where grain scars have a static orientation, the motion of dislocations parallel (climb) and perpendicular (glide) to grain scar corresponds to finite particle diffusivities.[32] This contribution to the ensemble-averaged diffusivity necessarily depends on the number of particles involved in the collective rearrangements that produce dislocation climb and glide. The collapse in **Fig. 8** follows from this model, however, the same collapse works especially well in the regime where grain scars do not have a static orientation and dislocation identity and their motion is ambiguous.

With an understanding of diffusion and defect structures in the liquid and dense crystal limits, we next examine all curvature and concentration dependent charge data (Q vs. $R/2a$) (**Fig. 9C**). A systematic transition occurs between the limiting cases (**Figs. 9A,B**). To develop a model of intermediate concentrations, we consider several aspects of the grain scar model. Increasing temperature increases the slope (from 0.41) in Eq. (6) for crystal states of Lennard-Jones particles on sphere surfaces,[33] so concentration may have an analogous role (with a reciprocal dependence). In addition, R_C is understood to depend on crystal elastic constants (in the zero temperature continuum model[18]), which can also be concentration dependent. However, we cannot expect low density crystal states of Brownian colloids to behave as a continuous elastic solid. With these analogies and limitations in mind, we combine Eqs. (5) and (6) to model the full η and R dependence of the total charge.

$$Q(R/2a,\eta) = \alpha(\eta)16\eta(R/2a)^2 + \chi \cdot 24\left[0.41(R-R_c)/2a+1/2\right] \qquad (7)$$

With only two adjustable parameters, χ and R_C, Eq. (7) accurately captures the BD simulated data (**Fig. 9C**). Placing χ at any other location within the grain scar term in Eq. (7) generally produces less a satisfactory fit and does not obviously contribute to its physical interpretation.

Several features in the η-dependence of the fit parameters (**Fig. 9D**) are easily contextualized by the limiting cases and yet reveal aspects of the intermediate transition. When $\chi=0$, Eq. (7) reduces to the liquid state expression (Eq. (5)), and when $\alpha(\eta)$ vanishes in crystal states and $\chi=1$, we recover the standard grain scar expression (Eq. (6)). In the fit parameters, χ transitions smoothly from zero to nearly one. Interestingly, this transition is not monotonic and has a maximum with $\chi>1$ at $\eta=0.73$, just past freezing. This maximum is indicative of 'proliferated' defects that are not part of zero temperature grain scars, nor are they associated with the baseline isotropic defect distribution, $\alpha(\eta)$. As already noted, R_C is not a well-defined parameter for hard discs (and undefinable for $\chi=0$). Future studies could investigate the energetic cost of defects in hard disc crystals to better understand R_C in relation to colloids on spherical surfaces.

To better understand the extra defects reflected in the fit parameter maxima just beyond freezing (**Fig. 9D**), we show local charge density renderings at the maximum χ value, which occurs for $\eta=0.73$ (**Fig. 9E**). Compared to grain scars at $\eta=0.8$ (**Fig. 9B**), the morphology of the time-averaged defect clusters is more rounded and without clear orientation at $\eta=0.73$. Since instantaneous tessellations still show 5-7-5 chains, the time averaged morphology change appears to occur as the result of fluctuations and motion in icosahedrally organized defect regions. As $R/2a$ decreases, defect regions get closer together until fluctuations bridge adjacent regions (appearing as pink spots linking darker red defect regions with icosahedral organization in **Fig. 9E**). Both the

fluctuations near freezing and interactions between defect regions appear to be mediated by rapid formation and annihilation of additional topological charges that account for $\chi>1$ in **Fig. 9D** (and changing R_C values).

The observed rapid formation and annihilation of individual defects (charges) occurs because the crystal tessellation is susceptible to particle displacements smaller than the lattice spacing. This means defects can transition between particle identities on the time scale of Brownian motion on a lattice site. For $\eta=0.8$, the defect number is small enough that defect dynamics are identifiable as dislocation climb and glide about static grain scars. However, near $\eta=0.73$ the substantial number of short-lived charges makes unambiguously identifying defects between instantaneous configurations impossible. Furthermore, since grain scars rapidly fluctuate in shape, orientation, and defect composition, identifying directions for relative defect motion is similarly ambiguous. Finally, the significant defect fluctuations occurring between grain scars also makes it difficult to identify icosahedral symmetry in instantaneous configurations. The time-average local charge density is necessary to see icosahedral symmetry near $\eta=0.73$.

These observations together suggest defect-mediated interactions between adjacent defect regions in crystalline states can break icosahedral symmetry, at least temporarily, and enable significant diffusion. Fluctuating defect clusters which interact across many particle lengths provide a compelling explanation for why, in **Fig 8C**, crystalline particles between the defect clusters can still exhibit inhomogeneous diffusivity. We expect that these collective fluctuations, which we characterize with Q/N, produce the apparent diffusive dynamics that we measure with D_L/D_0. With this context, we see that the effective collapse of $(D_L/D_0)/(Q/N)$ in **Fig 8A,B** reflects the intimate connection between the evolving sub-populations of defects and of highly diffusive particles. Ultimately, we find that diffusion in crystalline states is curvature dependent because it connected to defect-mediated dynamics that occur both within and between icosahedral defect regions (which eventually form grain scars at higher area fractions). However, the idea that thermally activated defects mediate collective elastic interactions to produce cooperative diffusive dynamics in spherical crystal states warrants further study of the particle-scale and defect-scale mechanisms involved.

Conclusions

Brownian dynamic simulations were performed for varying particle concentrations on 2D flat surfaces and spherical surfaces of varying relative curvature. Particles were modeled with short-range screened electrostatic repulsive potentials that behave as effective 2D hard spheres or hard disks, which is relevant for many interfacial colloidal systems. Diffusion was measured at short- and long- times from ensemble averaged mean squared displacements to capture single particle diffusion, liquid state self-diffusion, and diffusion through freezing in curved crystal states.

Liquid state self-diffusion is identical on flat and spherical surfaces with a concentration dependence captured by a simple model based on the first peak in the pair distribution function. Diffusion vanishes on flat surfaces upon freezing as expected but persists with a concentration and curvature dependence in crystal states on spherical surfaces. Similarly, the pair distribution function, local density distributions, and topological defect populations are also identical for liquid states on flat and spherical surfaces, but systematically vary with curvature upon freezing.

Diffusion in crystalline states on spherical surfaces does not clearly relate to local density metrics, but both its concentration and curvature dependence are easily captured by topological charge density. Topological charge density varies continuously between limits for isotropic liquid

states and dense crystal states with icosahedrally organized grain scars. Renderings and charge density scaling indicate curvature-dependent diffusivities in crystalline states on spherical surfaces reflect diffusion mediated by topological defects both within and between icosahedral pre-scar defect regions. Higher charge densities on higher curvature spheres appears to result from formation and annihilation of additional topological charges associated with interactions between fluctuating defect regions. Particles with higher diffusivities that are not necessarily located in defect regions appear mobile due to cooperative particle-scale mechanisms mediated by topological defects. Ultimately, understanding self-diffusion and topological defect mediated diffusion of spherical particles on spherical surfaces provides a basis to explore more complex cases involving particles with different shapes, interactions, and activities and surfaces with varying curvature landscapes.

Methods

Flat-case simulations use overdamped Langevin dynamics in HOOMD-blue,[37] which simplifies to standard Brownian dynamics.[38] Flat-case simulations use periodic boundary conditions with box sizes chosen to match the area fractions and particle numbers in corresponding spherical surface simulations. Spherical simulations use overdamped Langevin dynamics in LAMMPS[39] with RATTLE[31] to keep particles confined to surfaces while maintaining a consistent thermostat. In both engines, particles interact via a screened electrostatic potential matched to spherical silica colloids in water.[35] This potential has the form $U(r)=6051kT\exp(-280r)$. Each simulation runs for 300τ in total elapsed time, meaning that multiple-time-origin MSD curves can cover a maximum of 150τ. At least ten independent simulations were run for each case starting from randomly generated configurations for each combination of sphere radius, area fraction, and particle number. To remove artifacts from the periodic boundary conditions, flat-case MSD curves are calculated using the minimum image convention and in the ensemble center-of-mass frame. Spherical surface MSD curves were corrected for center-of-mass motion by bootstrapping the center of mass motion of many smaller sectors of particles on sphere surfaces.

Acknowledgments

References

1. Georgakilas, V.; Perman, J. A.; Tucek, J.; Zboril, R. Broad Family of Carbon Nanoallotropes: Classification, Chemistry, and Applications of Fullerenes, Carbon Dots, Nanotubes, Graphene, Nanodiamonds, and Combined Superstructures. *Chem Rev* **2015,** *115*, 4744-822.
2. Martin, R. L.; Smit, B.; Haranczyk, M. Addressing Challenges of Identifying Geometrically Diverse Sets of Crystalline Porous Materials. *J Chem Inf Model* **2012,** *52*, 308-18.
3. Caspar, D. L. D.; Klug, A. Physical Principles in the Construction of Regular Viruses. *Cold Spring Harbor Symposia on Quantitative Biology* **1962,** *27*, 1-24.
4. Korlach, J.; Schwille, P.; Webb, W. W.; Feigenson, G. W. Characterization of Lipid Bilayer Phases by Confocal Microscopy and Fluorescence Correlation Spectroscopy. *Proc Natl Acad Sci U S A* **1999,** *96*, 8461-6.
5. Xin, W.; Wu, H.; Grason, G. M.; Santore, M. M. Switchable Positioning of Plate-Like Inclusions in Lipid Membranes: Elastically Mediated Interactions of Planar Colloids in 2d Fluids. *Sci Adv* **2021,** *7*.
6. Jerri, H. A.; Torres-Díaz, I.; Zhang, L.; Impellizzeri, N.; Benczédi, D.; Bevan, M. A. Surface

Morphology-Enhanced Delivery of Bioinspired Eco-Friendly Microcapsules. *ACS Applied Materials & Interfaces* **2022,** *14*, 41499-41507.

7. Dinsmore, A. D.; Hsu, M. F.; Nikolaides, M. G.; Marquez, M.; Bausch, A. R.; Weitz, D. A. Colloidosomes: Selectively Permeable Capsules Composed of Colloidal Particles. *Science* **2002,** *298*, 1006-9.

8. Bowick, M. J.; Giomi, L. Two-Dimensional Matter: Order, Curvature and Defects. *Advances in Physics* **2009,** *58*, 449-563.

9. Shin, D.; Huang, T.; Neibloom, D.; Bevan, M. A.; Frechette, J. Multifunctional Liquid Marble Compound Lenses. *ACS Appl Mater Interfaces* **2019,** *11*, 34478-34486.

10. Aussillous, P.; Quere, D. Liquid Marbles. *Nature* **2001,** *411*, 924-7.

11. Goldstein, R. E. Green Algae as Model Organisms for Biological Fluid Dynamics. *Annu Rev Fluid Mech* **2015,** *47*, 343-375.

12. Kim, J.; Koo, B. K.; Knoblich, J. A. Human Organoids: Model Systems for Human Biology and Medicine. *Nat Rev Mol Cell Biol* **2020,** *21*, 571-584.

13. Kosterlitz, J. M.; Thouless, D. J. Ordering, Metastability and Phase Transitions in Two-Dimensional Systems. *Journal of Physics C: Solid State Physics* **1973,** *6*, 1181-1203.

14. Halperin, B. I.; Nelson, D. R. Theory of Two-Dimensional Melting. *Physical Review Letters* **1978,** *41*, 121-124.

15. Nelson, D. R.; Halperin, B. I. Dislocation-Mediated Melting in Two Dimensions. *Physical Review B* **1979,** *19*, 2457-2484.

16. Engel, M.; Anderson, J. A.; Glotzer, S. C.; Isobe, M.; Bernard, E. P.; Krauth, W. Hard-Disk Equation of State: First-Order Liquid-Hexatic Transition in Two Dimensions with Three Simulation Methods. *Phys Rev E Stat Nonlin Soft Matter Phys* **2013,** *87*, 042134.

17. Grason, G. M. Perspective: Geometrically Frustrated Assemblies. *The Journal of Chemical Physics* **2016,** *145*, 110901.

18. Bowick, M. J.; Nelson, D. R.; Travesset, A. Interacting Topological Defects on Frozen Topographies. *Physical Review B* **2000,** *62*, 8738-8751.

19. Bausch, A. R.; Bowick, M. J.; Cacciuto, A.; Dinsmore, A. D.; Hsu, M. F.; Nelson, D. R.; Nikolaides, M. G.; Travesset, A.; Weitz, D. A. Grain Boundary Scars and Spherical Crystallography. *Science* **2003,** *299*, 1716-8.

20. Guerra, R. E.; Kelleher, C. P.; Hollingsworth, A. D.; Chaikin, P. M. Freezing on a Sphere. *Nature* **2018,** *554*, 346-350.

21. Meng, G.; Paulose, J.; Nelson, D. R.; Manoharan, V. N. Elastic Instability of a Crystal Growing on a Curved Surface. *Science* **2014,** *343*, 634-7.

22. Wales, D. J.; McKay, H.; Altschuler, E. L. Defect Motifs for Spherical Topologies. *Physical Review B* **2009,** *79*, 224115.

23. Bahukudumbi, P.; Bevan, M. A. Imaging Energy Landscapes with Concentrated Diffusing Colloidal Probes. *J Chem Phys* **2007,** *126*, 244702.

24. Anekal, S. G.; Bevan, M. A. Self-Diffusion in Submonolayer Colloidal Fluids near a Wall. *J Chem Phys* **2006,** *125*, 34906.

25. Brady, J. F. The Long-Time Self-Diffusivity in Concentrated Colloidal Dispersions. *J. Fluid Mech.* **1994,** *272*, 109-133.

26. Lowen, H. Dynamical Criterion for Two-Dimensional Freezing. *Phys Rev E* **1996,** *53*, R29-R32.

27. Wang, Z.; Alsayed, A. M.; Yodh, A. G.; Han, Y. Two-Dimensional Freezing Criteria for Crystallizing Colloidal Monolayers. *J Chem Phys* **2010,** *132*, 154501.

28. Weiss, J. A.; Larsen, A. E.; Grier, D. G. Interactions, Dynamics, and Elasticity in Charge-Stabilized Colloidal Crystals. *The Journal of Chemical Physics* **1998,** *109*, 8659-8666.

29. Mondescu, R. P.; Muthukumar, M. Brownian Motion and Polymer Statistics on Certain Curved Manifolds. *Physical Review E* **1998,** *57*, 4411-4419.

30. Castro-Villarreal, P. Intrinsic and Extrinsic Measurement for Brownian Motion. *Journal of Statistical Mechanics: Theory and Experiment* **2014,** *2014*.

31. Paquay, S.; Kusters, R. A Method for Molecular Dynamics on Curved Surfaces. *Biophys J* **2016,** *110*, 1226-33.

32. Lipowsky, P.; Bowick, M. J.; Meinke, J. H.; Nelson, D. R.; Bausch, A. R. Direct Visualization of Dislocation Dynamics in Grain-Boundary Scars. *Nat Mater* **2005,** *4*, 407-11.

33. Vest, J. P.; Tarjus, G.; Viot, P. Glassy Dynamics of Dense Particle Assemblies on a Spherical Substrate. *J Chem Phys* **2018,** *148*, 164501.

34. Singh, N.; Sood, A. K.; Ganapathy, R. Observation of Two-Step Melting on a Sphere. *Proc Natl Acad Sci U S A* **2022,** *119*, e2206470119.

35. Zhang, J.; Zhang, Y.; Bevan, M. A. Spatially Varying Colloidal Phase Behavior on Multi-Dimensional Energy Landscapes. *J Chem Phys* **2020,** *152*, 054905.

36. Szamel, G.; Leegwater, J. A. Long-Time Self-Diffusion Coefficients of Suspensions. *Phys Rev A* **1992,** *46*, 5012-5019.

37. Anderson, J. A.; Glaser, J.; Glotzer, S. C. Hoomd-Blue: A Python Package for High-Performance Molecular Dynamics and Hard Particle Monte Carlo Simulations. *Computational Materials Science* **2020,** *173*, 109363.

38. Ermak, D. L.; McCammon, J. A. Brownian Dynamics with Hydrodynamic Interactions. *The Journal of Chemical Physics* **1978,** *69*, 1352-1360.

39. Thompson, A. P.; Aktulga, H. M.; Berger, R.; Bolintineanu, D. S.; Brown, W. M.; Crozier, P. S.; in 't Veld, P. J.; Kohlmeyer, A.; Moore, S. G.; Nguyen, T. D.; Shan, R.; Stevens, M. J.; Tranchida, J.; Trott, C.; Plimpton, S. J. Lammps - a Flexible Simulation Tool for Particle-Based Materials Modeling at the Atomic, Meso, and Continuum Scales. *Computer Physics Communications* **2022,** *271*, 108171.

Diffusion, Density, and Defects on Spheres

John E. Bond, Alex J. Yeh, John R. Edison, Michael A. Bevan†
Chemical & Biomolecular Engr., Johns Hopkins Univ., Baltimore, MD 21218 USA

Data Availability Statement

Data for this paper, including: example simulation scripts (python, bash) and input configurations (*.xyz* and *.gsd* files), custom analysis codes (Python) and analyzed values (*.npy*, *.json*, files) are available at "Data associated with the publication: Diffusion, Density, and Defects on Spheres" at https://doi.org/10.7281/T1/IZMSNX.

(During the peer review process, the data can be viewed at the non-permanent location: https://archive.data.jhu.edu/privateurl.xhtml?token=c495b1be-4d31-4617-b42a-486b4e4dc453)

---

† To whom correspondence should be addressed. email: mabevan@jhu.edu